1   **High definition DIC imaging uncovers transient stages of pathogen infection**

2   **cycles on the surface of human adult stem cell-derived intestinal epithelium**

3

4   Jorik M. van Rijn[a,*], Jens Eriksson[a,*], Jana Grüttner[b], Magnus Sundbom[c], Dominic-Luc

5   Webb[d], Per M. Hellström[d], Staffan G. Svärd[b], Mikael E. Sellin[a,#]

6

7   Affiliations:

8   [a] Science for Life Laboratory, Department of Medical Biochemistry and Microbiology,

9   Uppsala University, Uppsala, Sweden.

10   [b] Department of Cell and Molecular Biology, Uppsala University, Uppsala, Sweden.

11   [c] Department of Surgical Sciences, Uppsala University, Uppsala, Sweden.

12   [d] Department of Medical Sciences, Gastroenterology and Hepatology Unit, Uppsala

13   University, Uppsala, Sweden.

14   * Jorik M. van Rijn and Jens Eriksson contributed equally to this work. Author order was

15   determined on the basis of seniority.

16   #Correspondence: mikael.sellin@imbim.uu.se

17

Abstract

Interactions between individual pathogenic microbes and host tissues involve fast and dynamic processes that ultimately impact the outcome of infection. Using live-cell microscopy, these dynamics can be visualized to study e.g. microbe motility, binding and invasion of host cells, and intra-host-cell survival. Such methodology typically employs confocal imaging of fluorescent tags in tumor-derived cell line infections on glass. This allows high-definition imaging, but poorly reflects the host tissue's physiological architecture and may result in artifacts. We developed a method for live-cell imaging of microbial infection dynamics on human adult stem cell-derived intestinal epithelial cell (IEC) layers. These IEC monolayers are grown in alumina membrane chambers, optimized for physiological cell arrangement and fast, but gentle, differential interference contrast (DIC) imaging. This allows sub-second visualization of both microbial and epithelial surface ultrastructure at high resolution without using fluorescent reporters. We employed this technology to probe the behavior of two model pathogens, *Salmonella enterica* Typhimurium (*Salmonella*) and *Giardia intestinalis* (*Giardia*), at the intestinal epithelial surface. Our results reveal pathogen-specific swimming patterns on the epithelium, showing that *Salmonella* adheres to the IEC surface for prolonged periods before host-cell invasion, while *Giardia* uses circular swimming with intermittent attachments to scout for stable adhesion sites. This method even permits tracking of individual *Giardia* flagella, demonstrating that active flagellar beating and attachment to the IEC surface are not mutually exclusive. Thereby, this work describes a powerful, generalizable, and relatively inexpensive approach to study

40   dynamic pathogen interactions with IEC surfaces at high resolution and under near-

41   native conditions.

42

43   **Importance**

44   Knowledge of dynamic niche-specific interactions between single microbes and

45   host cells is essential to understand infectious disease progression. However, advances

46   in this field have been hampered by the inherent conflict between the technical

47   requirements for high resolution live-cell imaging on one hand, and conditions that best

48   mimic physiological infection niche parameters on the other. Towards bridging this

49   divide, we present methodology for differential interference contrast (DIC) imaging of

50   pathogen interactions at the apical surface of enteroid-derived intestinal epithelia,

51   providing both high spatial and temporal resolution. This alleviates the need for

52   fluorescent reporters in live-cell imaging and provides dynamic information about

53   microbe interactions with a non-transformed, confluent, polarized and microvilliated

54   human gut epithelium. Using this methodology, we uncover previously unrecognized

55   stages of *Salmonella* and *Giardia* infection cycles at the epithelial surface.

56

57   **Introduction**

58   Although infectious diseases of the intestine are often caused by large

59   populations of invading pathogens, disease progression and outcome are ultimately

60   dictated by the interactions of individual microbes with the host tissues. To characterize

61   the complex dynamics of these underlying interactions, live cell microscopy has become

62   the method of choice. However, it is intrinsically difficult to study dynamic microbe

3

63 interactions with internal host tissues such as the intestinal epithelium *in vivo*. The

64 resolution of *ex vivo*-based microscopy techniques often suffers from the complexity

65 and depth of intact tissues, resulting in the need for more phototoxic high-dosage

66 illumination or complex and expensive 2-photon setups. Therefore, researchers have

67 turned to transformed or immortalized cell lines to study intestinal epithelial infections in

68 cultured proxies of the gut epithelium. These cell lines often fail to recapitulate key

69 features of intestinal epithelial cell (IECs) layers, such as a densely-packed polarized

70 morphology, a microvilliated apical surface, and sensitivity to cell-death mechanisms,

71 but have nevertheless uncovered a wealth of information about pathogen infection

72 cycles (1–6). By contrast, the impact of physiologically relevant host cell and tissue

73 parameters on infection dynamics remains understudied.

74 In the past decade, cultured organoid models have been shown to provide a

75 powerful intermediate for this physiological gap between cell lines and intact primary

76 tissues. The central features of the gut epithelium are faithfully recapitulated in both

77 intestinal organoids derived from pluripotent stem cells (PSCs) (7, 8), and in so called

78 enteroids or colonoids derived from adult epithelial stem cells (ASCs) of small intestine

79 or colon, respectively (9, 10). Organoid models can be cultured in a variety of two- and

80 three-dimensional (2D and 3D) settings (11, 12) and retain non-transformed cell

81 behavior over time (13, 14).

82 Despite their potential, organoid models have so far only been sparsely used for

83 live cell imaging of intestinal infection processes (15–17). In our experience, this is a

84 result of the difficulty to adapt current imaging approaches from cell line infections to

85 accommodate the properties of physiologically grown organoid-derived epithelia. First,

4

86   while cell lines can be grown flat on glass culture ware for optimal working distance and

87   numerical aperture, intestinal organoid-derived IECs only develop into their natural

88   polarized arrangement when cultured within rich extracellular matrices (ECMs), or atop

89   permeable supports. The latter can be accommodated by ECM-coated transwell inserts

90   with permeable membranes of Polyethylene Terephthalate (PET) or similar polymers as

91   a 2D substrate (18, 19). Enteroid/Colonoid-derived IEC layers in such transwell inserts

92   can be efficiently cultured, differentiated, and infected by a variety of gut pathogens

93   (20–28), but are poorly compatible with live cell imaging. Secondly, non-transformed

94   cells are difficult to manipulate genetically, which complicates introduction of fluorescent

95   tags to visualize the host cell and its subcellular architecture by fluorescence microcopy.

96   Finally, in contrast to tumor-derived cell lines, non-transformed cells retain sensitive cell

97   death and stress signaling pathways, which makes them susceptible to phototoxicity

98   and other perturbations and introduces a need for gentle imaging conditions. Taken

99   together, these constraints have limited the applicability of live cell imaging to

100   characterize encounters of pathogens with the apical portion of non-transformed IEC

101   layers at high spatial and temporal resolution.

102   Here, we present a new method to visualize microbial infection cycle dynamics at

103   the apical surface of ASC-derived IEC layers under near-native conditions. To

104   overcome the imaging constraints introduced by PET transwells, we developed a

105   method to grow microvilliated human epithelium layers on ECM-coated alumina

106   membranes in 3D-printed imaging chambers. In addition, we omitted the need for

107   fluorescent tagging and high-dosage illumination by optimizing the conditions for high

108   resolution, live differential interference contrast (DIC) microscopy. The use of DIC rather

5

109   than more phototoxic fluorescent reporter approaches favors physiologic pathogen and

110   host cell behavior and allows simultaneous visualization of both individual microbes and

111   IEC surface ultrastructure without the need for channel switching. Finally, we used this

112   method to map *Salmonella enterica* Typhimurium (*Salmonella*), and *Giardia intestinalis*

113   (*Giardia*) infection cycles atop the epithelial surface and describe previously

114   unrecognized single-microbe behaviors during IEC attachment. Thereby, we show that

115   this imaging methodology enables detailed, dynamic studies of both microbe and host

116   cell behavior at the interface of gut infection, adaptable even to genetically non-tractable

117   microorganisms.

118

119   **Results**

120   ***An alumina membrane chamber enables high-definition live cell DIC imaging at***

121   ***the apical border of intestinal epithelial cell layers***

122   We developed a method for live cell imaging of microbe interactions with non-

123   transformed human ASC-derived intestinal epithelial cell layers, aiming to combine i)

124   high structural definition, ii) high temporal resolution, iii) gentle imaging conditions to

125   avoid phototoxicity and the need for fluorescent reporters, and iv) a confluent, polarized

126   IEC arrangement. To achieve this, we sought to improve upon the constraints presented

127   by PET transwell supports to DIC imaging (Fig 1A). Specifically, the PET membrane

128   depolarizes light, the pores in the membranes diffract light, and the plastic membrane

129   holder prevents close approach of the microscope objective to the apical side of the

130   IECs, thereby constraining the working distance and numerical aperture. Therefore, a

131   suitable alternative to PET membranes should not introduce optical interference for

6

132   imaging within the visual spectrum, but like PET membranes should be permeable to

133   permit efficient epithelial cell polarization. In addition, the membrane holder should allow

134   close proximity of both the objective and condenser to the epithelial surface to optimize

135   the numerical aperture of the system.

136   This led us to evaluate membranes of anodized aluminium oxide (alumina) as a

137   candidate substrate. Alumina forms a dense honeycomb-like structure with parallel,

138   sub-diffraction limit sized pores (Fig S1A), and is optically transparent when wet. Unlike

139   for PET membranes, the pores cannot be distinguished by light microscopy and the

140   alumina does not depolarize transmitted light (Fig S1B). Although alumina membranes

141   poorly support cell adhesion, various adhesion-enhancing surface modifications have

142   been reported for this material (29–31). We found that surface hydroxylation followed by

143   sequential coating with poly-L-lysine and Matrigel enabled efficient attachment and

144   expansion of human ASC-derived IECs atop the alumina membranes (Fig S1C; see

145   methods for details). Furthermore, IECs grown on coated alumina membranes

146   developed into confluent, highly polarized monolayers, reflecting *in vivo* epithelium

147   architecture (Fig S1D). To hold the alumina membrane in place during cell culture, we

148   designed a 3D-printable plastic chamber (Fig 1B). The design of the chamber can easily

149   be adapted to alternative applications, and design files are freely available for download

150   (will be available upon publication). Like a regular transwell, the chamber creates a cell

151   culture area in the middle, but the height of the chamber was kept slim to match the

152   working distance of a water-dipping objective, thereby removing air-liquid interfaces

153   within the light path. In addition, the chamber allows the objective and especially the

154   condenser to be placed in close proximity to the sample, hence maximizing the

7

155   utilization of the condenser´s numerical aperture and thus improving the lateral

156   resolution of DIC imaging.

157   To test if this alumina membrane chamber (AMC) and upright microscope setup

158   indeed improved the quality of live DIC imaging of epithelial infection, we compared this

159   system to the existing PET transwell supports. Human IEC monolayers were grown and

160   differentiated atop PET transwells, or in AMCs, and the apical compartment was

161   infected with wild-type *Salmonella*. The PET transwells were imaged using either a

162   standard inverted DIC microscope and an oil-immersion objective (Fig 1C), or the PET

163   membrane cut out from the holder for imaging with the upright water-dipping objective

164   setup (Fig 1D). Infections in the AMCs were imaged in parallel using the same upright

165   system (Fig 1E). As expected, the contrast and resolution of both the apical IEC surface

166   and the *Salmonella* was poor for PET transwells imaged through the inverted

167   microscope (Fig 1F-G), but markedly improved through the water-dipping upright

168   system (Fig 1H-I). However, residual optical interference from the PET membrane was

169   still evident, resulting in image blurring. Moreover, the need to cut-out the PET

170   membrane prior to imaging complicated sample handling, increased risk of mechanical

171   cell damage, and caused the loose membrane to float with convection currents in the

172   imaging medium, which prevented stable image acquisition over time.

173   The AMC markedly improved on all these imaging issues by providing a stable

174   surface, minimizing the optical interference from membrane pores, and allowing easy

175   handling underneath the water-dipping objective. As such, DIC imaging of live, infected

176   IEC monolayers in AMCs showed distinct contrast of *Salmonella* atop the cell surface

177   (Fig 1J). When focusing on the IEC surface itself, we observed clearly demarcated cell-

8

178   cell junctions and a remarkable roughness made up of contrasting punctae (Fig 1K),

179   suggestive of a densely microvilliated surface. To correlate the live DIC image with the

180   IEC surface topology, we disassembled non-infected and *Salmonella*-infected AMCs

181   and imaged the epithelial monolayers therein also by scanning electron microscopy

182   (SEM). This provided a powerful, near-correlative setup, as SEM analysis could be

183   done on the same AMC samples used for live DIC. SEM images captured at similar

184   magnification validated the appearance of the apical epithelial surface in live DIC mode,

185   both with respect to the macro-topology of cell junctions, the slight height differences

186   between cells, and the distinctly patterned apical surface (compare figure 1K and L). At

187   higher SEM magnification, we observed a richly microvilliated surface (Fig 1M), with

188   preserved binding of *Salmonella* to the host cells (Fig 1N).

189   In conclusion, the combination of an upright water-dipping objective microscope

190   and the novel AMC provide a system for simultaneous high definition DIC imaging of

191   both microbe- and host cell- features at the apical surface of human intestinal epithelial

192   cell layers. This approach does not require the use of fluorescent dyes or labeled

193   markers, and allows for convenient semi-correlative SEM on samples fixed at the end of

194   live cell imaging.

195

196   ***Resolving sub second-scale microbial motility patterns along the apical surface***

197   ***of human intestinal epithelium***

198   Pathogenic gut microbes often use flagellar motility to reach and explore the

199   epithelial surface. Motile pathogen behaviors have typically been studied atop artificial

200   surfaces (e.g. plastic or glass) (3, 32), or occasionally under more physiological

201   conditions (e.g. atop tissue explants (33)). However, under the latter conditions the

202   imaging method relies on fluorescent reporters and high-intensity illumination that come

203   at the price of phototoxicity, and may alter the processes under study, or do not permit

204   simultaneous surface structure visualization. The AMC setup presented here should be

205   ideally suited to study authentic pathogen motility patterns at the IEC surface under

206   minimally perturbing conditions. To leverage this possibility, we explored motility of two

207   microbes atop IEC monolayers grown in AMCs: the smaller bacterial pathogen

208   *Salmonella*, and the larger protozoan parasite *Giardia*.

209   Peritrichous flagella-driven *Salmonella* motility physically constrains stretches of

210   the bacterial swim path atop surfaces – a phenomenon called near-surface swimming

211   (NSS) (3). Using DIC imaging alone, we could successfully follow *Salmonella* NSS

212   along the apical surface of the epithelium with high frame rates (up to ~30 frames/sec)

213   at modest light intensity, and with simultaneous visualization of apical epithelial topology

214   (Fig 2A, top row panel). Although bacterial NSS could easily be tracked manually based

215   on the DIC images alone, greyscale images cannot be readily thresholded for

216   automated downstream analysis by particle tracking software, as would be the norm for

217   fluorescence imaging (Fig S2A; (34)). We therefore incorporated a squared temporal

218   median (TM^2) post-processing filter (see methods) to extract bacterial NSS information

219   from the background of the relatively static apical IEC topology. The resulting filtered

220   image stack enabled both segmentation of motile bacteria and automated particle

221   tracking without the use of fluorescent markers (Fig 2A - bottom row panels, movie will

222   be provided upon publication). Automated tracking of *Salmonella* NSS in the TM^2

223   filtered stack showed a variety of curved tracks with a mean speed of 34.7 µm/s (Fig 2B,

224   Fig S2C) and mean turning angle of ~14.68°/15 µm clockwise (Fig S2E), corresponding

225   to its flagella's counterclockwise spin (35, 36). Reassessment of this pattern by

226   fluorescence imaging resulted in broadly similar tracks (Fig S2A,C), but importantly did

227   not allow simultaneous visualization of epithelial surface topology. These observations

228   validate and extend previous studies of *Salmonella* motility (3, 33, 36–38), by mapping

229   *Salmonella* NSS parameters atop a physiologically arranged epithelial surface and

230   under minimally perturbing conditions.

231   *Giardia* trophozoites feature four pairs of flagella, and use motility to swiftly

232   approach the intestinal epithelium, followed by stable attachment using a ventral disk

233   (39, 40). *Giardia* free-swimming motility in medium involves flexion of the caudal portion

234   of the parasite body (32). On flat surfaces (i.e. glass), *Giardia* adapt the swimming

235   mode to planar motility, largely driven by the flagella. Planar motility in this context is

236   defined by a swimming pattern with the ventral disk continuously in the same plane as

237   the attachment surface (32, 41). As these *Giardia* motility characteristics remain inferred

238   from more simplistic experimental conditions (40), we performed live DIC imaging of

239   early *Giardia* motility atop IEC monolayers within AMCs. Again, we could

240   simultaneously visualize the IEC surface and individual *Giardia* trophozoites, and follow

241   parasite movements at a variety of frame rates (Fig 2C, top row panels). The lower

242   contrast and less predictable swim paths noted for these bigger protozoans, as

243   compared to *Salmonella*, were not well suited for automated particle tracking. However,

244   an unsquared temporal median filtering (TM) step aided robust manual segmentation

245   and tracking of *Giardia* motility (Fig 2C - bottom row panels, movie will be provided upon

246   publication). This revealed epithelium-proximal swimming in curved or circular tracks

11

247   with a mean speed of 38.6 µm/s (Fig 2D, Fig S2D) and an almost straight mean turning

248   angle of 0.41°/15 µm, but with a large standard deviation in both the clockwise and

249   counterclockwise direction (Fig S2F). We validated these findings also by fluorescence

250   imaging of mNeonGreen-labelled *Giardia* and automated particle tracking (Fig S2B,D).

251   The speed values aligned well with the maximal speeds measured for *Giardia* during

252   free-swimming in media (up to ~40µm/s; (32)). This indicates that when first

253   approaching a polarized microvilliated epithelium, *Giardia* sustains maximal swim speed

254   for a significant period after switching to planar 2D motility.

255   Taken together, we demonstrate that DIC imaging in AMCs provides a powerful

256   solution for resolving microbial motility patterns atop a human intestinal epithelial cell

257   layer. Specifically, this methodology simultaneously captures both apical IEC layer

258   topology and single microbe behaviors at high frame rates, does not require fluorescent

259   labelling, and as such avoids both potential problems with reporter toxicity/phototoxicity,

260   as well as the temporal delays that come with switching between multiple imaging

261   channels. Moreover, the AMC imaging technology will allow in-depth analysis of how

262   microbial motility on the epithelial surface is impacted by physiologically relevant

263   surface features (e.g. crevices formed at cell-cell junctions, extruding IECs etc.).

264

265   ***Longer-term imaging reveals a previously unrecognized Salmonella Typhimurium***

266   ***infection cycle stage atop the epithelial surface***

267   Following NSS, *Salmonella* can adhere to the epithelial surface through a

268   combination of transient interactions via dedicated adhesins and/or flagella, and stable

269   docking to the plasma membrane via type-III-secretion system-1 (TTSS-1) (42–45).

270   Docking of the TTSS-1 tip subsequently permits the translocation of bacterial effector

271   proteins into the host cell cytoplasm (1). A rich body of work in epithelial cell line models

272   has shown that this leads to the near-instantaneous induction of large actin-dependent

273   membrane ruffles and swift *Salmonella* invasion of the targeted cell (1). However,

274   recent work has also shown that the induced invasion structure phenotype is dependent

275   on the context of the host cell, and suggests a relation between invasion phenotype and

276   host cell polarization status (46). It therefore remains less well understood how the

277   physiological properties of intact non-transformed epithelia may impact *Salmonella*

278   infection cycle stage(s) at the host cell surface.

279   To survey the longer-term fate(s) of *Salmonella* on IECs, we performed one-hour

280   infections of AMC chamber-grown IEC monolayers. In the resulting movies, we

281   observed an abundance of non-motile bacteria on the surface of the IEC monolayer (Fig

282   3A). The accumulation of bacteria on the cell surface occurred in a time-dependent

283   manner, and they most often remained attached for the duration of the experiment. On

284   occasion a bacterium was seen to clearly detach, indicating that not all bacteria

285   successfully formed stable docking interactions with the epithelial surface. Surprisingly,

286   stable immobilization of the bacteria only rarely led to successful invasion of the

287   monolayer (Fig 3A). Instead, this analysis uncovered prolonged lingering of *Salmonella*

288   atop the epithelial surface as the predominant behavior, even enabling bacterial division

289   of attached bacteria upon the apical surface (Fig S3). This contrasts sharply to similar

290   experiments in non-polarized epithelial cell line models, where ruffle-dependent

291   *Salmonella* entry begins within seconds to minutes post-attachment (example movie will

292   be provided upon publication) (3, 46). Nevertheless, IEC invasion could still be detected

13

293   in the AMC-grown IEC monolayers, albeit at lower-than-expected frequency. Some

294   bacteria disappeared from the focal plane without obvious morphological changes to the

295   IEC surface (Fig 3B, top row panels). We could for this category not unequivocally

296   distinguish between sudden detachment or IEC invasion in the absence of overt surface

297   perturbation. In other cases, we observed unambiguous *Salmonella* invasion through a

298   small digitated IEC surface rim transiently formed around the bacterium (Fig 3B - middle

299   row panels, movie will be provided upon publication), or through somewhat more

300   pronounced donut-like ruffles which begun resembling those elicited in *Salmonella*-

301   infected polarized MDCK cells (Fig 3B, bottom row panels) (46–48).

302   Successful entry of the bacterium was occasionally followed by prompt neighbor-

303   coordinated extrusion of the targeted IEC from the monolayer (Fig 3C). The extrusion

304   phenotype and timeframe corresponded well with the extrusions we previously reported

305   in *Salmonella*-infected 3D enteroids (15), and which have also been observed *in vivo*

306   (49–51). Again, using DIC imaging alone, the morphological changes in both the

307   extruding IEC and the neighboring cells could be traced over time (Fig 3C).

308   In conclusion, our results show that imaging of epithelial infection within AMCs

309   opens up new avenues for the microscope-aided study of bacterial behavior at the

310   apical border of a human IEC layer, compatible with both short (sub-second) and long

311   (hours or more) time scales. By employing this technology, we find that *Salmonella* do

312   not invade a physiologically arranged human IEC layer as easily as what has been

313   described for tumor-derived cell line infection models. Instead, stable and prolonged

314   bacterial colonization of the IEC surface constitutes a significant infection cycle stage,

315   which only for a fraction of the bacteria converts into productive IEC invasion. The

316 molecular and physiological basis for these observations constitutes an intriguing area

317 for future research.

318

319 ***Giardia alternates between rapid swimming and intermittent attachment during***

320 ***local surface exploration***

321 Earlier reports of *Giardia* behavior on glass have described the trophozoites' pre-

322 attachment swimming pattern as circular movements, largely driven by beating of the

323 anterior and ventral flagella and steered by lateral bending of the caudal region (32, 41).

324 Although the eventual attachment of *Giardia* has been validated in numerous reports

325 (40, 52), and also in epithelial cell line cultures (5, 53), exploratory trophozoite behavior

326 that leads to successful stable attachment has not yet been studied atop an intact

327 epithelial surface.

328 Therefore, we homed in on individual *Giardia* swim tracks in IEC layer regions

329 that harbored both moving and stably adhered trophozoites (Fig 4A, attached *Giardia*

330 indicated by arrows in top panel). The subset of motile *Giardia* was observed to swim in

331 circular tracks which gradually shifted their position on top of the monolayer (Fig 4B).

332 From these tracks, the link speed was calculated as the displacement divided by the

333 time interval between two subsequent frames. Unlike for the patterns described on

334 glass (32, 41), we observed a remarkably high link speed variation for this pre-

335 attachment swimming, with an average of 31.98 µm/s ranging up to ~155 µm/s (Fig S4).

336 Over time, these tracks scanned repeatedly over a local region of the epithelium (Fig

337 4A, track).

338   To study how this swimming behavior relates to IEC attachment, we carefully

339   followed the link speed variation over each full track. This revealed that trophozoites in

340   planar swimming mode occasionally slowed down to a full stop on certain areas of the

341   monolayer (Fig 4B, black arrows). Interestingly, we also found that trophozoites often

342   repeatedly visited a certain location, coming to a brief stop with each pass across that

343   particular stretch of surface (Fig 4B, white arrow). This suggests that some areas of the

344   IEC monolayer may possess properties more favorable to attachment than others. It

345   seems plausible that the highly repetitive circular pre-attachment swim patterns we

346   observe will maximize the parasite's ability to find such ideal attachment sites within a

347   given epithelial region.

348   With four pairs of flagella and an adhesive ventral disk, *Giardia* behavior at a

349   surface is the result a complicated interplay of propulsion and adhesive forces. Aside

350   from their role in propulsion, flagellar movement has been described to influence correct

351   positioning of the adhesive disk on the attachment surface, although the exact

352   mechanism of that process remains a topic of discussion (32, 52). To test if our AMC

353   imaging setup would allow studies of individual flagella movements within the context of

354   epithelial infection, we imaged individual *Giardia* atop the IEC monolayer at high frame

355   rate. We found that DIC imaging alone was indeed sufficient to distinguish the

356   movement of individual flagella on intermittently attached trophozoites (Fig 4C, top

357   panel). Application of the TM filter further facilitated manual segmentation of individual

358   flagella (Fig 4C - middle panel, movie will be provided upon publication), and the

359   imaging resolution was sufficient to indicate the movement of all four pairs of flagella

360   over time (Fig 4C, middle and bottom panel). This allowed us to determine that all of the

16

361   anterior, posterolateral, and ventral flagella exhibit continued movement also in

362   intermittently attached *Giardia* on IEC monolayers. Consequently, intermittent *Giardia*

363   pausing at the IEC surface is not caused by the temporary cessation of flagellar beating.

364   This finding also illustrates the power of the AMC imaging technology to resolve

365   dynamic host-pathogen interactions under near-native conditions even with subcellular

366   resolution.

367

368   **Discussion**

369   Recent work has shown that intestinal organoid-derived monolayers grown on

370   permeable supports provide a physiologically relevant culture model for host-pathogen

371   interaction, applicable to both bacteria (21–26, 28), parasites (27), and viruses (20). In

372   this context, organoids bridge the gap between the complexity and polarized nature of

373   the epithelium encountered *in vivo* and the convenient (yet sometimes

374   misrepresentative) properties of continuous cultured cell lines. Furthermore, 2D

375   organoid cultures offer an attractive alternative to 3D culture specifically for studies of

376   microbe interactions with the apical cell surface. The latter can be microinjected (15, 54,

377   55), fragmented (56), or inverted (57), but because of the 3D-topology these structures

378   are better suited for population-scale dynamics than single-microbe behavior in a stable

379   apical plane. While live-cell imaging of microbe dynamics has been published on

380   monolayers of continuous cell lines (3, 47, 58) and to an extent in microinjected 3D

381   enteroids (15), dynamic behaviors of microbes at the surface of a physiologically

382   arranged human intestinal epithelium remain poorly investigated. We show that this

383   short-coming can be explained by the inherent conflict between the technical

17

384   prerequisites for high-definition light microscopy (e.g. a short working distance, a thin

385   specimen, and an optically inert substrate) and the current best practices for

386   establishment of polarized IEC layer cultures.

387   Therefore, we here developed a custom imaging chamber based on a coated

388   alumina membrane substrate. This AMC is compatible with water-dipping objective

389   imaging to maximize optical resolution, while the alumina membrane has optical

390   properties superior to permeable plastic cell culture supports. With these improvements

391   to the ASC-derived IEC monolayer culture system, we present an optimized method for

392   high-definition imaging of host - microbe interactions at the apical surface of a confluent,

393   polarized, non-transformed, human gut epithelium. Finally, we used this technique to

394   uncover previously unknown behaviors of both *Salmonella* and *Giardia* on IEC

395   monolayers.

396   Our AMC imaging model allows tracing of the behavior of individual *Salmonella*

397   cells over time from the moment they come in proximity to the apical cell surface.

398   Previous work using continuous cell lines and *in vivo* infection models have shown that

399   flagella-dependent *Salmonella* motility drives the approach towards host cells (37, 59)

400   and initiates subsequent NSS-behavior in search of suitable entry sites (3, 33). Our

401   findings regarding *Salmonella*'s curved NSS atop IEC monolayers (Fig 2A,B; Fig

402   S2A,C,E) agree with this model of approach. However, in contrast to observations in

403   e.g. HeLa cells, we found that successful binding to the IEC monolayer does not

404   necessarily lead to prompt ruffle-mediated invasion (Fig 3A). Rather, we observed that

405   the bacteria often remain attached without invading within an hour post-infection. From

406   our current observations, it is not clear if this binding is reversible and adhesin-

18

407 dependent, or rather comprises irreversible TTSS-1-mediated docking (42). The

408 molecular obstacle(s) that make polarized non-transformed IECs more challenging to

409 invade than typical cell lines constitutes an intriguing area for further enquiry. The

410 prolonged bacterial attachment also suggests an additional biologically relevant

411 epithelial colonization stage in the infection cycle of *Salmonella*, in apparent analogy to

412 attaching-effacing enteropathogens that use the epithelial surface as a primary

413 colonization niche (60).

414 Nevertheless, we still observed *Salmonella* invasion of IECs (Fig 3B), albeit at

415 lower-than-expected frequency and often through entry structures that were smaller and

416 more transient than previously noted for infections of flat-growing cell lines (example

417 movie will be provided upon publication; (46)). This is in line with the more 'discreet'

418 mode of *Salmonella* TTSS-1-dependent IEC invasion described in the intact mouse

419 intestine (46). In agreement with literature (17, 49–51, 61–64), we also observed that

420 successful invasion of the monolayer can lead to immediate extrusion of the infected

421 IEC (Fig 3C). When combined with tools for targeted epithelial cell differentiation,

422 bacterial and mammalian genetics, we expect the AMC imaging technology to provide a

423 framework for deciphering bacterial IEC invasion mechanics and the IEC extrusion

424 response in a near-native epithelial context.

425 Previous studies of *Giardia* infections have shown that the motile trophozoites

426 can attach to both inert substrates like glass (40) and to microvilliated cell surfaces *in*

427 *vivo* (65) and in culture (5). Research on interaction dynamics of *Giardia* with inert

428 substrates have shown that flagellar motility is essential for motility, cell division, and

429 selection of suitable attachment sites (32, 41, 52, 66, 67), although this behavior has not

19

430   yet been studied in real time on live cells. We here report the first study of *Giardia*

431   swimming on top of cultured cells, and on polarized IEC monolayers at that. In general

432   agreement with earlier studies on glass (32), we found that *Giardia* exhibits circular,

433   planar swimming above the attachment surface. Specifically, we found that *Giardia*

434   planar swimming speeds average around 30-40 µm/s with short bursts of up to 155

435   µm/s (Fig S4). These speeds are much higher than pre-attachment swimming that has

436   been characterized before on glass (32, 41, 67–69). Furthermore, we see circular

437   swimming interceded by short stretches of straight swimming (Fig 4A). Finally, we show

438   that trophozoite planar swimming along the epithelial surface leads to intermittent,

439   transient, attachments to the host cells (Fig 4B). Some of these attachments were seen

440   to repeatedly occur in the same location on the epithelial surface. Therefore, our results

441   suggest that *Giardia* planar swimming is geared towards a local surface-scanning

442   pattern, optimized to select a suitable attachment site within a given region. The circular

443   swimming pattern could aid in this process by repeatedly visiting promising sites of

444   adhesion, until an unknown threshold of stable adhesion is reached. Earlier work on

445   glass has elegantly shown that flagellar beating is instrumental to the planar swimming

446   behavior of *Giardia,* although the respective contribution of the anterior, posterolateral,

447   and ventral pair is still a matter of debate (32, 41). Strikingly, temporal median filtering in

448   our study resolved the continued movements of both anterior, posterolateral, and

449   ventral flagella in intermittently surface-attached *Giardia* (Fig 4C). Although we cannot

450   directly measure attachment force, this suggests that the transient *Giardia* pauses

451   during surface search can be explained by ventral disk or ventrolateral flange (65, 70)

452   engagement with the surface, rather than by an on-off behavior of flagellar propulsion.

20

453   As the AMC imaging method can be used to study both the overall swim patterns and

454   the movement of individual flagella, this technique is ideally suited to characterize the

455   complete spectrum of *Giardia* (and other parasite) behaviors atop intestinal epithelia.

456   Finally, the AMC imaging method can be adapted to accommodate a variety of

457   different host cell types and microbes. As we have shown that the coated alumina

458   membrane supports the growth of ASC-derived human enteroid monolayers, the current

459   system can likely be used to grow a variety of embryonic stem cell-, iPSC- and ASC-

460   derived epithelia. This would allow for high-definition imaging of microbial interactions

461   with any stem cell-derived human epithelium culture (e.g. airway, mammary gland,

462   stomach, or bladder epithelium, see (12) for a comprehensive overview). As ASC-

463   derived organoids retain the locational and functional identity (71) from the donor

464   material, this methodology could also be used to study the impact of congenital

465   disorders of the epithelium (like some forms of Very Early Onset Inflammatory Bowel

466   Disease) on microbial infection. Lastly, recent studies have reported an adapted

467   chamber for ASC-derived intestinal organoid monolayer co-culture with gut anaerobes

468   (26). Innovations like this open the door to even better modeling of both resident and

469   pathogenic microbes under even more physiologically accurate conditions. However, it

470   remains difficult to study dynamic interactions with the host epithelium in this context, as

471   most gut microbiota strains cannot yet be genetically modified to incorporate fluorescent

472   markers. Our AMC approach to image microbe interactions with the intestinal epithelium

473   without fluorescence could here provide a stepping stone for dynamic analysis of host

474   epithelium - microbiota interactions in the coming years.

475

476 **Materials & methods**

477 ***Ethics statement***

478   Human jejunal ASC-derived enteroids were generated from resected tissue

479 acquired from routine bariatric surgery, following prior informed consent. All personal

480 information was pseudonymized, and the patients' identities were unknown to

481 researchers working with the tissue samples. These procedures were approved by the

482 local governing body (Etikprövningsmyndigheten, Uppsala, Sweden) under license

483 number 2010-157 with addendums 2010-157-1 (2018-06-13) and 2020-05754 (2020-

484 10-26)

485

486 ***Alumina Membrane Chambers***

487   The Alumina Membrane Chambers (AMCs) for 13 mm alumina Whatman

488 Anodisc membranes with 0.2 µm pores (GE Healthcare, Little Chalfont, UK) were

489 designed in-house using FreeCAD v0.19 (https://www.freecadweb.org). The chamber

490 comprises a bottom holder and top cover, which fit together using a friction press fit to

491 hold the alumina membrane in place, with culture medium compartments generated on

492 each side of the membrane. The top cover contains a groove to hold a silicone gasket

493 (product number 527-9790, RS Components Ltd. Corby, UK) with inner diameter of 7.65

494 millimeter in place. AMC design files are available for non-commercial use and will be

495 provided upon publication. The AMC designs were printed using an Original Prusa

496 MINI+ (Prusa Research, Prague, Czech Republic) 3D printer with a 0.4 mm nozzle and

497 a layer height of 0.2 mm. The AMCs were printed in 1.75 mm, clear, natural PLA

498 filament (prod. number 832-0210, RS Components Ltd.).

22

499

Enteroid culture

501   Human jejunal enteroids were established and cultured as described previously

502   (15, 17). Briefly, pieces of intestinal resections were washed thoroughly in ice-cold PBS

503   and epithelial crypts were subsequently dissociated using Gentle Cell Dissociation

504   Reagent (STEMCELL Technologies, Vancouver, BC, Canada) by nutating at 4°C for 30

505   minutes followed by trituration. The resulting epithelial fragments were filtered through a

506   70 μm cell strainer and crypt-enriched fractions suspended in 50 μl Matrigel (Corning,

507   Corning, NY, USA) domes in a 24 well plate. The embedded crypts were cultured in

508   OGM (IntestiCult Organoid Growth Medium (Human), STEMCELL Technologies) with

509   100 U/ml penicillin/streptomycin (Thermo Fisher (Gibco), Waltham, MA, USA) at 37°C

510   and 5% CO_2. Growth medium was refreshed every 2-3 days.

511   For maintenance of human enteroids, the structures were passaged weekly at a

512   ratio of circa 1:8 by mechanical dissociation. The Matrigel domes were manually broken

513   up by pipetting with Gentle Dissociation Reagent and then washed once with

514   DMEM/F12/1.25% BSA. The resulting suspended enteroids were disrupted by triturating

515   15-20 times with a 200ul pipet tip. Following disruption, enteroid fragments were again

516   suspended in 50 μl Matrigel:Intesticult at the ratio 3:1, divided over 3 domes per well in

517   a 24 well plate, and cultured at 37°C and 5% CO_2.

518

Enteroid-derived IEC monolayer culture

520   Human IEC monolayers were cultured on either 24-well transparent polyethylene

521   terephthalate (PET) tissue culture inserts with 0.4 μm pores (Sarstedt, Nümbrecht,

522 Germany) or 13 mm diameter alumina Whatman Anodisc membranes. The PET

523 transwell inserts were coated with 40× diluted Matrigel in PBS for one hour at room

524 temperature prior to use. After this time, the coating was completely removed and the

525 cell suspension was immediately added to the transwell inserts. The alumina

526 membranes were coated with extracellular matrix as well, but required more extensive

527 pretreatment. First, the alumina membranes were soaked in 30% H_2O_2 for 1 hour at

528 room temperature to add negatively charged hydroxyl groups to the surface (30) and

529 allow protein binding. Then, the alumina membranes were washed in sterile dH_2O and

530 incubated in 0.1 mg/ml poly-L-lysine (Sigma-Aldrich, Stockholm, Sweden) in dH_2O for 5

531 minutes to prepare the surface for Matrigel coating. After poly-L-lysine coating, the

532 membranes were air-dried in a laminar flow cabinet for ~2 hours or overnight. Finally,

533 the alumina membranes were soaked in 40× diluted Matrigel in dH_2O for 1 hour, and

534 air-dried again. After coating, the membranes were mounted within AMCs.

535 Human enteroids were dissociated into single cell suspensions as described

536 before (17). Briefly, circa one well of enteroids per membrane was dissociated into

537 single cells at day 7 after passaging. The enteroids were first taken up from the Matrigel

538 in Gentle Dissociation Reagent, then washed in PBS/1.25% BSA, and dissociated into

539 single cells using TrypLE Express (Thermo Fisher (Gibco)) for 5-10 minutes at 37°C.

540 Cells were then spun down at 300 rcf for 5 minutes and resuspended in OGM+Y (Rho

541 kinase inhibitor Y-27632 (10 μM), Sigma). Finally, the cells were counted manually and

542 $3.0×10^5$ cells where seeded into the apical compartment of PET transwells in 150 μl

543 (600 μl medium in bottom compartment, 24-well plate wells), or into the apical

544 compartment of AMCs in 75 μl (600 μl medium in the bottom compartment, 12 well plate

24

545   wells). The monolayers typically grew confluent in 2-4 days, whereafter the cells were

546   differentiated towards an enterocyte phenotype by deprivation of Wnt-signalling for 4-5

547   days. The medium for differentiation consisted of DMEM/F12 supplemented with 5% R-

548   Spondin1 conditioned medium (home made from Cultrex 293T R-spondin1-expressing

549   cells, R&D Systems, MN, USA), 10% Noggin conditioned medium (home made with

550   HEK293-mNoggin-Fc cells, kindly provided by Prof. Hans Clevers, Utrecht University),

551   50 ng/ml mouse recombinant EGF (Sigma-Aldrich), 1X B27 supplement (Gibco), 1.25

552   mM N-acetyl cysteine, and 100 U/ml penicillin/streptomycin (9, 10).

553

554   **Salmonella Typhimurium strain, plasmid, culture, and infection**

555   All *Salmonella* infections in this study were performed with *Salmonella enterica*

556   serovar Typhimurium, SL1344 (SB300) (72). For validation by standard fluorescence

557   microscopy, the strain carried a pFPV-mCherry (rpsM-mCherry; Addgene plasmid

558   number 20956) plasmid directing constitutive mCherry expression (73). As reported

559   previously, expression of this mCherry construct did not influence motility or invasive

560   behavior of *Salmonella* SL1344. For IEC monolayer infections, *Salmonella* inoculi were

561   grown in LB/0.3 M NaCl (Sigma-Aldrich) for 12 h overnight with 50 µg/ml ampicillin. The

562   following day, a 1:20 dilution was subcultured in LB/0.3 M NaCl without antibiotics for 4

563   h. For subsequent infection of monolayer cultures, the 4h inoculum was diluted to

564   1.0×10^8 CFU/ml in DMEM/F12 (Thermo Fisher (Gibco)) without antibiotics of which 10

565   ul was used for each infection, resulting in 1.0×10^6 CFU per monolayer.

566

567 ***Giardia intestinalis culture and infection***

568   *Giardia intestinalis* isolate WB, clone C6 (ATCC 30957) was used in this study.

569 For validation by standard fluorescence microscopy, a modified *Giardia* line

570 constitutively expressing mNeonGreen was generated (see below). *Giardia* trophozoites

571 were grown at 37°C in 10 ml flat plastic tubes (Thermo Fisher Nunc, MA, USA) or 50ml

572 tubes (Sarstedt, Germany) filled with TYDK medium (also known as modified TYI-S-33

573 or Keister's medium) (74), supplemented with 10% heat-inactivated bovine serum

574 (Gibco, Thermo Fisher MA, United States). All materials used in the TYDK medium

575 were purchased from Sigma-Aldrich (MO, USA) unless otherwise stated. For IEC

576 monolayer infections, *Giardia* trophozoites were grown until approximately 70%

577 confluence and washed once with TYDK to remove dead cells. Further, trophozoites

578 were incubated on ice (12 min), counted and pelleted by centrifugation (800 x g, 10 min,

579 4°C). Cells were washed once in 1 ml DMEM/F12 (Thermo Fisher (Gibco)), centrifuged

580 and diluted to 2×10^7 or 4×10^7 trophozoites/ml using DMEM/F12 of which 10µl were

581 used for infection, resulting in 2×10^5 - 4×10^5 trophozoites per monolayer.

582

583 ***mNeonGreen plasmid construction and Giardia trophozoite transfection***

584   To visualize *Giardia* trophozoites on IEC monolayers also by fluorescence

585 microscopy, we created a trophozoite strain constitutively expressing mNeonGreen

586 under the control of the beta-giardin promoter. The mNeonGreen gene was PCR-

587 amplified from the pNCS-mNeonGreen plasmid (Allele Biotechnology, CA, USA) and

588 the beta-giardin 5'UTR and 3'UTR regions were amplified from genomic DNA of the WB

589 isolate (see Table S1). The PCR fragments were fused by overlap extension PCR and

26

590   cloned into the integration vector pPacV-Integ-HA-C (75) using XbaI/PacI restriction

591   sites. *Giardia* trophozoites were electroporated as previously described (76). Transgenic

592   parasites that had the mNeonGreen expression cassette integrated on the chromosome

593   were selected by adding puromycin (50μg/ml) to the culture medium approximately 16 h

594   after transfection. To ensure homogeneous mNeonGreen expression in the culture, we

595   created a clonal trophozoite population from the original mNeonGreen stable

596   transfectant population using serial dilution. Briefly, the original trophozoite culture was

597   diluted in TYDK and seeded as single cells into the wells of a 96-well plate. Wells

598   reaching 70–80% confluence were selected and grown in 10 ml tubes containing TYDK.

599   After the establishment of the clonal mNeonGreen strains the trophozoites were grown

600   without antibiotics.

601

602   ***Fixed IEC monolayer imaging***

603   Differentiated IEC monolayers grown in AMCs were fixed in 4% PFA for 30 min

604   and permeabilized with 0.1% Triton X-100 for 10 minutes. Then, the cells were stained

605   with phalloidin-AF488 (Thermo Fisher) and 4′,6-Diamidino-2-phenylindole

606   dihydrochloride (DAPI, Sigma-Aldrich) counterstain for 30 min in PBS. Subsequently,

607   the alumina membrane with cells was removed from the plastic membrane holder,

608   washed, and mounted under a 0.17 μm coverslip in Mowiol 4-88 (Sigma-Aldrich). The

609   samples were imaged on a Zeiss LSM700 inverted point-scanning microscope system

610   with a 63X/1.4 NA oil immersion objective using a voxel size of 70.6 nm (x,y) and 0.54

611   μm (z-sections).

612

613 ***Live cell infection imaging***

614   Live cell imaging was performed on an inverted Nikon Ti-eclipse microscope

615 (Nikon Corporation, Tokyo, Japan) with a 60X/1.4 NA Nikon PLAN APO objective (0.19

616 mm WD), Nikon condenser (0.52 NA, LWD), and Andor Zyla sCMOS camera

617 (Abingdon, Oxfordshire, England) with pixel size of 108 nm for Fig 1C,D,F-I and a

618 custom upright microscope for all other experiments. The upright microscope is a

619 custom-build, largely based on the Thorlabs Cerna upright microscopy system (Newton,

620 NJ, USA) with a heated 60X/1.0 NA Nikon CFI APO NIR objective (2.8 mm WD) and a

621 Nikon D-CUO DIC Oil Condenser (1.4 NA) controlled by Micro-Manager 2.0-gamma

622 (77). Images were acquired with an ORCA-Fusion camera (model number C14440-

623 20UP, Hamamatsu photonics, Hamamatsu City, Japan), with a final pixel size of 109

624 nm. Transmitted light was supplied by a 530 nm Thorlabs LED (M530L3) to minimize

625 phototoxicity and chromatic aberrations. The microscope chamber was maintained at

626 37°C in a moisturized 5% CO_2 atmosphere and an objective heater was used

627 additionally. Samples in AMCs were mounted in 35 mm glass-bottom dishes (Cellvis,

628 Mountain View, CA, USA) in 3 ml DMEM/F12 without antibiotics in the microscope's

629 light path, and allowed to equilibrate for 30 minutes. Then, *Salmonella* or *Giardia* were

630 added in pre-made dilutions directly underneath the objective, and imaging was started

631 immediately with <20 ms exposure times for DIC imaging and <50 ms for fluorescence

632 imaging.

633

634 ***SEM imaging***

635   For SEM analysis of AMC-grown monolayers, *Salmonella* infected IEC

636 monolayers were fixed at 40 minutes post-infection and compared with uninfected

637 controls. To fix the samples, the monolayers were gently washed once with PBS and

638 fixed at 4°C overnight with 2.5% glutaraldehyde (Sigma) in 0.1M PHEM buffer (60mM

639 PIPES, 25mM HEPES, 10mM EGTA, and 4mM MgSO4·7H20, pH 6.9). Prior to SEM

640 imaging, the samples were dehydrated in series of graded ethanol, critical point dried

641 (Leica EM CPD300) and coated with 5 nm platinum (Quorum Q150T-ES sputter coater).

642 The sample morphology was examined by field-emission scanning electron microscope

643 (FESEM; Carl Zeiss Merlin) using in-lens and in-chamber secondary electron detectors

644 at accelerating voltage of 4 kV and probe current of 100 pA.

645

646 ***Image processing***

647   The acquired microscopy images were processed with Fiji (78). DIC images in

648 figures 2, 3, 4, and S3 were filtered to acquire an even field of illumination by

649 subtracting a (30-pixel sigma) gaussian blurred projection from the original. Where

650 indicated, a temporal median (TM) filter was used to extract quickly moving structures

651 (e.g. motile *Salmonella*, *Giardia*, and moving flagella) by subtracting the median

652 projection of the time stack from each individual frame. To enable automated particle

653 tracking of moving *Salmonella* in DIC time series, pixel values of the signed 32-bit TM

654 filtered stacks were squared to convert both 'dark' and 'light' bacteria in the TM-filtered

655 image to positive values. These TM^2-filtered images were used for automated particle

656   tracking. Both automated and manual particle tracking was performed with Trackmate

657   for ImageJ v6.0.1 (34).

658

659   ***Tracking analysis and statistics***

660   Data analysis was performed with R (79) and RStudio (80) and packages

661   available from the Comprehensive R Archive Network (CRAN, https://cran.r-

662   project.org/). Tracking statistics were exported from Trackmate, and actual frame

663   intervals were obtained from the image metadata using the Cellocity python package

664   (81) to correct for variations between frames which would be reflected in inaccurate link

665   speeds. Subsequently, the track data was formatted and plotted in R with the 'tidyverse'

666   (82) package. Tracks with a mean speed of >100 µm/s were manually confirmed to be

667   false positives of automated tracking, and therefore excluded from analysis. Track angle

668   changes for DIC-tracked swimming paths were calculated using functions based on the

669   'trajr' package (83) with an interval of three links. For the *Salmonella* swimming tracks,

670   only tracks with a mean speed of >5 µm/s were included in the analysis to filter away

671   most non-motile bacteria. The three-link angle change was divided by the distance

672   travelled from the reference link to calculate the angle change per micron. To aid

673   interpretation of this parameter, the angle change / micron was normalized to angle

674   change / 15 micron, the average distance travelled in 3 links. Other supporting

675   packages for R include 'ggpubr', 'rstatix', 'ggbeeswarm', 'viridis', 'ggridges', and 'scales'.

676

677 **Acknowledgements**

690

691 **Contributions:** Conceptualization: JMvR, JE, MES; Methodology: JMvR, JE, JG, MES;

692 Investigation: JMvR, JE, JG; Formal analysis: JMvR, JE, JG, MES; Resources: MS,

693 DLW, PMH, SGS, MES; Supervision: SGS, MES; Project administration: MS, DLW,

694 PMH, SGS, MES; Funding acquisition: SGS, PMH, MES; Visualization: JMvR, JG;

695 Writing - Original Draft: JMvR, MES; Writing - Reviewing & Editing: all authors.

696

697 **Conflict of interest:** The authors have no competing interests to declare.

698

699 **References**

700 1. Hume PJ, Singh V, Davidson AC, Koronakis V. 2017. Swiss Army Pathogen: The

701   Salmonella Entry Toolkit. Frontiers in Cellular and Infection Microbiology 7:1–13.

702 2. Kellermann M, Scharte F, Hensel M. 2021. Manipulation of Host Cell Organelles by

703   Intracellular Pathogens. Int J Mol Sci 22:6484.

704 3. Misselwitz B, Barrett N, Kreibich S, Vonaesch P, Andritschke D, Rout S, Weidner

705   K, Sormaz M, Songhet P, Horvath P, Chabria M, Vogel V, Spori DM, Jenny P,

706   Hardt WD. 2012. Near surface swimming of salmonella Typhimurium explains

707   target-site selection and cooperative invasion. PLoS Pathogens 8:e1002810.

708 4. Chang Y-Y, Enninga J, Stévenin V. 2021. New methods to decrypt emerging

709   macropinosome functions during the host-pathogen crosstalk. Cell Microbiol

710   23:e13342.

711 5. Sousa MC, Gonçalves CA, Bairos VA, Poiares-Da-Silva J. 2001. Adherence of

712   Giardia lamblia trophozoites to Int-407 human intestinal cells. Clin Diagn Lab

713   Immunol 8:258–265.

714 6. Dowd GC, Mortuza R, Bhalla M, Van Ngo H, Li Y, Rigano LA, Ireton K. 2020.

715   *Listeria monocytogenes* exploits host exocytosis to promote cell-to-cell spread.

716   Proc Natl Acad Sci USA 117:3789–3796.

717 7. Spence JR, Mayhew CN, Rankin SA, Kuhar MF, Vallance JE, Tolle K, Hoskins EE,

718   Kalinichenko VV, Wells SI, Zorn AM, Shroyer NF, Wells JM. 2011. Directed

719 differentiation of human pluripotent stem cells into intestinal tissue in vitro. Nature

720 470:105–110.

721 8. Wells JM, Spence JR. 2014. How to make an intestine. Development 141:752–

722 760.

723 9. Sato T, Stange DE, Ferrante M, Vries RGJ, Van Es JH, Van Den Brink S, Van

724 Houdt WJ, Pronk A, Van Gorp J, Siersema PD, Clevers H. 2011. Long-term

725 expansion of epithelial organoids from human colon, adenoma, adenocarcinoma,

726 and Barrett's epithelium. Gastroenterology 141:1762–1772.

727 10. Sato T, Vries RG, Snippert HJ, van de Wetering M, Barker N, Stange DE, van Es

728 JH, Abo A, Kujala P, Peters PJ, Clevers H. 2009. Single Lgr5 stem cells build

729 crypt-villus structures in vitro without a mesenchymal niche. Nature 459:262–265.

730 11. Dedhia PH, Bertaux-Skeirik N, Zavros Y, Spence JR. 2016. Organoid Models of

731 Human Gastrointestinal Development and Disease. Gastroenterology 150:1098–

732 1112.

733 12. Kim J, Koo B-K, Knoblich JA. 2020. Human organoids: model systems for human

734 biology and medicine. Nature Reviews Molecular Cell Biology 21:571–584.

735 13. Blokzijl F, de Ligt J, Jager M, Sasselli V, Roerink S, Sasaki N, Huch M, Boymans

736 S, Kuijk E, Prins P, Nijman IJ, Martincorena I, Mokry M, Wiegerinck CL,

737 Middendorp S, Sato T, Schwank G, Nieuwenhuis EES, Verstegen MMA, van der

738 Laan LJW, de Jonge J, IJzermans JNM, Vries RG, van de Wetering M, Stratton

739   MR, Clevers H, Cuppen E, van Boxtel R. 2016. Tissue-specific mutation

740   accumulation in human adult stem cells during life. Nature 538:260–264.

741 14. Sato T, Clevers H. 2013. Growing self-organizing mini-guts from a single intestinal

742   stem cell: mechanism and applications. Science 340:1190–1194.

743 15. Geiser P, Di Martino ML, Samperio Ventayol P, Eriksson J, Sima E, Al-Saffar AK,

744   Ahl D, Phillipson M, Webb D-L, Sundbom M, Hellström PM, Sellin ME. 2021.

745   Salmonella enterica Serovar Typhimurium Exploits Cycling through Epithelial Cells

746   To Colonize Human and Murine Enteroids. mBio 12:e02684-20.

747 16. Kim M, Fevre C, Lavina M, Disson O, Lecuit M. 2021. Live Imaging Reveals

748   Listeria Hijacking of E-Cadherin Recycling as It Crosses the Intestinal Barrier. Curr

749   Biol 31:1037-1047.e4.

750 17. Samperio Ventayol P, Geiser P, Di Martino ML, Florbrant A, Fattinger SA, Walder

751   N, Sima E, Shao F, Gekara NO, Sundbom M, Hardt W-D, Webb D-L, Hellström

752   PM, Eriksson J, Sellin ME. 2021. Bacterial detection by NAIP/NLRC4 elicits prompt

753   contractions of intestinal epithelial cell layers. Proc Natl Acad Sci U S A

754   118:e2013963118.

755 18. Moon C, VanDussen KL, Miyoshi H, Stappenbeck TS. 2013. Development of a

756   primary mouse intestinal epithelial cell monolayer culture system to evaluate

757   factors that modulate IgA transcytosis. Mucosal immunology 7:818–828.

758   19. VanDussen KL, Marinshaw JM, Shaikh N, Miyoshi H, Moon C, Tarr PI, Ciorba MA,

759   Stappenbeck TS. 2014. Development of an enhanced human gastrointestinal

760   epithelial culture system to facilitate patient-based assays. Gut 64:911–920.

761   20. Ettayebi K, Crawford SE, Murakami K, Broughman JR, Karandikar U, Tenge VR,

762   Neill FH, Blutt SE, Zeng X-L, Qu L, Kou B, Opekun AR, Burrin D, Graham DY,

763   Ramani S, Atmar RL, Estes MK. 2016. Replication of human noroviruses in stem

764   cell–derived human enteroids. Science 353:1387–1393.

765   21. In J, Foulke-Abel J, Zachos NC, Hansen A-M, Kaper JB, Bernstein HD, Halushka

766   M, Blutt S, Estes MK, Donowitz M, Kovbasnjuk O. 2016. Enterohemorrhagic

767   Escherichia coli Reduces Mucus and Intermicrovillar Bridges in Human Stem Cell-

768   Derived Colonoids. Cellular and Molecular Gastroenterology and Hepatology 2:48-

769   62.e3.

770   22. Kim R, Attayek PJ, Wang Y, Furtado KL, Tamayo R, Sims CE, Allbritton NL. 2019.

771   An in vitro intestinal platform with a self-sustaining oxygen gradient to study the

772   human gut/microbiome interface. Biofabrication 12:015006.

773   23. Koestler BJ, Ward CM, Fisher CR, Rajan A, Maresso AW, Payne SM. 2019.

774   Human Intestinal Enteroids as a Model System of Shigella Pathogenesis. Infect

775   Immun 87:e00733-18.

776   24. Nakamoto N, Sasaki N, Aoki R, Miyamoto K, Suda W, Teratani T, Suzuki T, Koda

777   Y, Chu P-S, Taniki N, Yamaguchi A, Kanamori M, Kamada N, Hattori M, Ashida H,

778   Sakamoto M, Atarashi K, Narushima S, Yoshimura A, Honda K, Sato T, Kanai T.

779   2019. Gut pathobionts underlie intestinal barrier dysfunction and liver T helper 17

780   cell immune response in primary sclerosing cholangitis. Nat Microbiol 4:492–503.

781   25. Ranganathan S, Doucet M, Grassel CL, Delaine-Elias B, Zachos NC, Barry EM.

782   2019. Evaluating Shigella flexneri Pathogenesis in the Human Enteroid Model.

783   Infect Immun 87:e00740-18.

784   26. Sasaki N, Miyamoto K, Maslowski KM, Ohno H, Kanai T, Sato T. 2020.

785   Development of a Scalable Coculture System for Gut Anaerobes and Human

786   Colon Epithelium. Gastroenterology 159:388-390.e5.

787   27. Wilke G, Funkhouser-Jones LJ, Wang Y, Ravindran S, Wang Q, Beatty WL,

788   Baldridge MT, VanDussen KL, Shen B, Kuhlenschmidt MS, Kuhlenschmidt TB,

789   Witola WH, Stappenbeck TS, Sibley LD. 2019. A Stem-Cell-Derived Platform

790   Enables Complete Cryptosporidium Development In Vitro and Genetic Tractability.

791   Cell Host & Microbe 26:123-134.e8.

792   28. Nickerson KP, Llanos-Chea A, Ingano L, Serena G, Miranda-Ribera A, Perlman M,

793   Lima R, Sztein MB, Fasano A, Senger S, Faherty CS. 2021. A Versatile Human

794   Intestinal Organoid-Derived Epithelial Monolayer Model for the Study of Enteric

795   Pathogens. Microbiol Spectr e0000321.

796   29. Charles-Orszag A, Tsai FC, Bonazzi D, Manriquez V, Sachse M, Mallet A, Salles

797   A, Melican K, Staneva R, Bertin A, Millien C, Goussard S, Lafaye P, Shorte S, Piel

798   M, Krijnse-Locker J, Brochard-Wyart F, Bassereau P, Duménil G. 2018. Adhesion

799   to nanofibers drives cell membrane remodeling through one-dimensional wetting.

800   Nature Communications 9:4450.

801   30.   Formentín P, Catalán, Pol L, Fernández-Castillejo S, Solà R, Marsal LF. 2018.

802   Collagen and fibronectin surface modification of nanoporous anodic alumina and

803   macroporous silicon for endothelial cell cultures. Journal of Biological Engineering

804   12:1–9.

805   31.   van Dongen SFM, Maiuri P, Piel M. 2014. Chapter 11 - A Reagent-Based Dynamic

806   Trigger for Cell Adhesion, Shape Change, or Cocultures, p. 171–184. *In* Piel, M,

807   Théry, M (eds.), Methods in Cell Biology. Academic Press.

808   32.   Lenaghan SC, Davis CA, Henson WR, Zhang Z, Zhang M. 2011. High-speed

809   microscopic imaging of flagella motility and swimming in Giardia lamblia

810   trophozoites. PNAS 108:E550–E558.

811   33.   Furter M, Sellin ME, Hansson GC, Hardt WD. 2019. Mucus Architecture and Near-

812   Surface Swimming Affect Distinct Salmonella Typhimurium Infection Patterns along

813   the Murine Intestinal Tract. Cell Reports 27:2665-2678.e3.

814   34.   Tinevez J-Y, Perry N, Schindelin J, Hoopes GM, Reynolds GD, Laplantine E,

815   Bednarek SY, Shorte SL, Eliceiri KW. 2017. TrackMate: An open and extensible

816   platform for single-particle tracking. Methods 115:80–90.

817   35.   Spöring I, Martinez VA, Hotz C, Schwarz-Linek J, Grady KL, Nava-Sedeño JM,

818   Vissers T, Singer HM, Rohde M, Bourquin C, Hatzikirou H, Poon WCK, Dufour YS,

819   Erhardt M. 2018. Hook length of the bacterial flagellum is optimized for maximal

820   stability of the flagellar bundle. PLOS Biology 16:e2006989.

821 36. Cooper KG, Chong A, Kari L, Jeffrey B, Starr T, Martens C, McClurg M, Posada

822   VR, Laughlin RC, Whitfield-Cargile C, Garry Adams L, Bryan LK, Little SV, Krath

823   M, Lawhon SD, Steele-Mortimer O. 2021. Regulatory protein HilD stimulates

824   Salmonella Typhimurium invasiveness by promoting smooth swimming via the

825   methyl-accepting chemotaxis protein McpC. Nat Commun 12:348.

826 37. Horstmann JA, Zschieschang E, Truschel T, de Diego J, Lunelli M, Rohde M, May

827   T, Strowig T, Stradal T, Kolbe M, Erhardt M. 2017. Flagellin phase-dependent

828   swimming on epithelial cell surfaces contributes to productive Salmonella gut

829   colonisation. Cell Microbiol 19:e12739.

830 38. Otte S, Ipiña EP, Pontier-Bres R, Czerucka D, Peruani F. 2021. Statistics of

831   pathogenic bacteria in the search of host cells. Nat Commun 12:1990.

832 39. Einarsson E, Ma'ayeh S, Svärd SG. 2016. An up-date on Giardia and giardiasis.

833   Current Opinion in Microbiology 34:47–52.

834 40. Hagen KD, McInally SG, Hilton ND, Dawson SC. 2020. Chapter Two - Microtubule

835   organelles in Giardia, p. 25–96. *In* Ortega-Pierres, MG (ed.), Advances in

836   Parasitology. Academic Press.

837 41. Lenaghan SC, Chen J, Zhang M. 2013. Modeling and analysis of propulsion in the

838   multiflagellated micoorganism Giardia lamblia. Phys Rev E Stat Nonlin Soft Matter

839   Phys 88:012726.

38

840   42. Misselwitz B, Kreibich SK, Rout S, Stecher B, Periaswamy B, Hardt WD. 2011.

841   Salmonella enterica serovar typhimurium binds to hela cells via fim-mediated

842   reversible adhesion and irreversible type three secretion system 1-mediated

843   docking. Infection and Immunity 79:330–341.

844   43. Lara-Tejero M, Galán JE. 2009. Salmonella enterica serovar Typhimurium

845   pathogenicity island 1-encoded type III secretion system translocases mediate

846   intimate attachment to nonphagocytic cells. Infection and Immunity 77:2635–2642.

847   44. Gerlach RG, Jäckel D, Stecher B, Wagner C, Lupas A, Hardt W-D, Hensel M.

848   2007. Salmonella Pathogenicity Island 4 encodes a giant non-fimbrial adhesin and

849   the cognate type 1 secretion system. Cell Microbiol 9:1834–1850.

850   45. Horstmann JA, Lunelli M, Cazzola H, Heidemann J, Kühne C, Steffen P, Szefs S,

851   Rossi C, Lokareddy RK, Wang C, Lemaire L, Hughes KT, Uetrecht C, Schlüter H,

852   Grassl GA, Stradal TEB, Rossez Y, Kolbe M, Erhardt M. 2020. Methylation of

853   Salmonella Typhimurium flagella promotes bacterial adhesion and host cell

854   invasion. Nat Commun 11:2013.

855   46. Fattinger SA, Böck D, Martino MLD, Deuring S, Ventayol PS, Ek V, Furter M,

856   Kreibich S, Bosia F, Müller-Hauser AA, Nguyen BD, Rohde M, Pilhofer M, Hardt W-

857   D, Sellin ME. 2020. Salmonella Typhimurium discreet-invasion of the murine gut

858   absorptive epithelium. PLOS Pathogens 16:e1008503.

859   47. Jepson MA, Kenny B, Leard AD. 2001. Role of sipA in the early stages of

860   Salmonella typhimurium entry into epithelial cells. Cellular Microbiology 3:417–426.

861   48. Kommnick C, Lepper A, Hensel M. 2019. Correlative light and scanning electron

862   microscopy (CLSEM) for analysis of bacterial infection of polarized epithelial cells.

863   Scientific reports 9:17079.

864   49. Knodler LA, Vallance BA, Celli J, Winfree S, Hansen B, Montero M, Steele-

865   Mortimer O. 2010. Dissemination of invasive Salmonella via bacterial-induced

866   extrusion of mucosal epithelia. Proc Natl Acad Sci U S A 107:17733–17738.

867   50. Sellin ME, Müller AA, Felmy B, Dolowschiak T, Diard M, Tardivel A, Maslowski KM,

868   Hardt WD. 2014. Epithelium-intrinsic NAIP/NLRC4 inflammasome drives infected

869   enterocyte expulsion to restrict salmonella replication in the intestinal mucosa. Cell

870   Host and Microbe 16:237–248.

871   51. Laughlin RC, Knodler LA, Barhoumi R, Payne HR, Wu J, Gomez G, Pugh R,

872   Lawhon SD, Bäumler AJ, Steele-Mortimer O, Adams LG. 2014. Spatial segregation

873   of virulence gene expression during acute enteric infection with Salmonella

874   enterica serovar Typhimurium. mBio 5:e00946-13.

875   52. House SA, Richter DJ, Pham JK, Dawson SC. 2011. Giardia Flagellar Motility Is

876   Not Directly Required to Maintain Attachment to Surfaces. PLoS Pathog

877   7:e1002167.

878   53. Hansen WR, Fletcher DA. 2008. Tonic Shock Induces Detachment of Giardia

879   lamblia. PLoS Negl Trop Dis 2:e169.

880   54. Wilson SS, Tocchi A, Holly MK, Parks WC, Smith JG. 2015. A small intestinal
881   organoid model of non-invasive enteric pathogen-epithelial cell interactions.
882   Mucosal Immunol 8:352–361.

883   55. Bartfeld S, Bayram T, van de Wetering M, Huch M, Begthel H, Kujala P, Vries R,
884   Peters PJ, Clevers H. 2015. In vitro expansion of human gastric epithelial stem
885   cells and their responses to bacterial infection. Gastroenterology 148:126-136.e6.

886   56. Zhao X, Li C, Liu X, Chiu MC, Wang D, Wei Y, Chu H, Cai J-P, Chan IH-Y, Wong
887   KK-Y, Chan JF-W, To KK-W, Yuen KY, Zhou J. 2021. Human Intestinal Organoids
888   Recapitulate Enteric Infections of Enterovirus and Coronavirus. Stem Cell Reports
889   16:493–504.

890   57. Co JY, Margalef-Català M, Li X, Mah AT, Kuo CJ, Monack DM, Amieva MR. 2019.
891   Controlling Epithelial Polarity: A Human Enteroid Model for Host-Pathogen
892   Interactions. Cell Reports 26:2509-2520.e4.

893   58. Perrett CA, Jepson MA. 2009. Regulation of Salmonella-induced membrane ruffling
894   by SipA differs in strains lacking other effectors. Cellular Microbiology 11:475–487.

895   59. Stecher B, Hapfelmeier S, Müller C, Kremer M, Stallmach T, Hardt W-D. 2004.
896   Flagella and chemotaxis are required for efficient induction of Salmonella enterica
897   serovar Typhimurium colitis in streptomycin-pretreated mice. Infect Immun
898   72:4138–4150.

899   60. Woodward SE, Krekhno Z, Finlay BB. 2019. Here, there, and everywhere: How

900   pathogenic Escherichia coli sense and respond to gastrointestinal biogeography.

901   Cellular Microbiology 21:e13107.

902   61. Crowley SM, Han X, Allaire JM, Stahl M, Rauch I, Knodler LA, Vallance BA. 2020.

903   Intestinal restriction of Salmonella Typhimurium requires caspase-1 and caspase-

904   11 epithelial intrinsic inflammasomes. PLoS pathogens 16:e1008498.

905   62. Holly MK, Han X, Zhao EJ, Crowley SM, Allaire JM, Knodler LA, Vallance BA,

906   Smith JG. 2020. Salmonella enterica infection of murine and human enteroid-

907   derived monolayers elicits differential activation of epithelial-intrinsic

908   inflammasomes. Infection and Immunity 88:00017–00020.

909   63. Fattinger SA, Geiser P, Samperio Ventayol P, Di Martino ML, Furter M, Felmy B,

910   Bakkeren E, Hausmann A, Barthel-Scherrer M, Gül E, Hardt W-D, Sellin ME. 2021.

911   Epithelium-autonomous NAIP/NLRC4 prevents TNF-driven inflammatory

912   destruction of the gut epithelial barrier in Salmonella-infected mice. Mucosal

913   Immunol 14:615–629.

914   64. Rauch I, Deets KA, Ji DX, von Moltke J, Tenthorey JL, Lee AY, Philip NH, Ayres

915   JS, Brodsky IE, Gronert K, Vance RE. 2017. NAIP-NLRC4 Inflammasomes

916   Coordinate Intestinal Epithelial Cell Expulsion with Eicosanoid and IL-18 Release

917   via Activation of Caspase-1 and -8. Immunity 46:649–659.

918   65. Holberton DV. 1973. Fine structure of the ventral disk apparatus and the

919   mechanism of attachment in the flagellate Giardia muris. J Cell Sci 13:11–41.

920   66. Dawson SC. 2010. An insider's guide to the microtubule cytoskeleton of Giardia.

921   Cell Microbiol 12:588–598.

922   67. Campanati L, Holloschi A, Troster H, Spring H, Souza W de, Monteiro-Leal LH.

923   2002. Video-microscopy observations of fast dynamic processes in the protozoon

924   Giardia lamblia. Cell Motility 51:213–224.

925   68. Chen J, Lenaghan SC, Zhang M. 2012. Analysis of dynamics and planar motion

926   strategies of a swimming microorganism — Giardia lamblia, p. 4204–4209. *In* 2012

927   IEEE International Conference on Robotics and Automation.

928   69. Lisicki M, Velho Rodrigues MF, Goldstein RE, Lauga E. 2019. Swimming

929   eukaryotic microorganisms exhibit a universal speed distribution. eLife 8:e44907.

930   70. Erlandsen SL, Russo AP, Turner JN. 2004. Evidence for Adhesive Activity of the

931   Ventrolateral Flange in Giardia lamblia. Journal of Eukaryotic Microbiology 51:73–

932   80.

933   71. Middendorp S, Schneeberger K, Wiegerinck CL, Mokry M, Akkerman RDL, Van

934   Wijngaarden S, Clevers H, Nieuwenhuis EES. 2014. Adult stem cells in the small

935   intestine are intrinsically programmed with their location-specific function. Stem

936   Cells 32:1083–1091.

937   72. Hoiseth SK, Stocker BA. 1981. Aromatic-dependent Salmonella typhimurium are

938   non-virulent and effective as live vaccines. Nature 291:238–239.

939   73. Drecktrah D, Levine-Wilkinson S, Dam T, Winfree S, Knodler LA, Schroer TA,

940   Steele-Mortimer O. 2008. Dynamic Behavior of Salmonella-Induced Membrane

941   Tubules in Epithelial Cells. Traffic 9:2117–2129.

942   74. Keister DB. 1983. Axenic culture of Giardia lamblia in TYI-S-33 medium

943   supplemented with bile. Trans R Soc Trop Med Hyg 77:487–488.

944   75. Morf L, Spycher C, Rehrauer H, Fournier CA, Morrison HG, Hehl AB. 2010. The

945   transcriptional response to encystation stimuli in Giardia lamblia is restricted to a

946   small set of genes. Eukaryot Cell 9:1566–1576.

947   76. Jerlström-Hultqvist J, Stadelmann B, Birkestedt S, Hellman U, Svärd SG. 2012.

948   Plasmid vectors for proteomic analyses in Giardia: purification of virulence factors

949   and analysis of the proteasome. Eukaryot Cell 11:864–873.

950   77. Edelstein AD, Tsuchida MA, Amodaj N, Pinkard H, Vale RD, Stuurman N. 2014.

951   Advanced methods of microscope control using µManager software. 2. Journal of

952   Biological Methods 1:1-e10.

953   78. Schindelin J, Arganda-Carreras I, Frise E, Kaynig V, Longair M, Pietzsch T,

954   Preibisch S, Rueden C, Saalfeld S, Schmid B, Tinevez J-Y, White DJ, Hartenstein

955   V, Eliceiri K, Tomancak P, Cardona A. 2012. Fiji: an open-source platform for

956   biological-image analysis. Nature methods 9:676–682.

957   79. R Core Team. 2021. R: A Language and Environment for Statistical Computing. R

958   Foundation for Statistical Computing, Vienna, Austria.

959   80. RStudio Team. 2021. RStudio: Integrated Development Environment for R.

960   RStudio, PBC, Boston, MA.

961   81. Eriksson J, Styrström D, Sellin M. 2021. Cellocity: A Python package for analysis of

962   confluent cell layer dynamics. Journal of Open Source Software 6:2818.

963   82. Wickham H, Averick M, Bryan J, Chang W, McGowan LD, François R, Grolemund

964   G, Hayes A, Henry L, Hester J, Kuhn M, Pedersen TL, Miller E, Bache SM, Müller

965   K, Ooms J, Robinson D, Seidel DP, Spinu V, Takahashi K, Vaughan D, Wilke C,

966   Woo K, Yutani H. 2019. Welcome to the tidyverse. Journal of Open Source

967   Software 4:1686.

968   83. McLean DJ, Volponi MAS. 2018. trajr: An R package for characterisation of animal

969   trajectories. Ethology 124:440–448.

970

971   **Figure legends**

972   **Figure 1. High-definition live cell DIC imaging of IEC monolayer infections in a**

973   **novel alumina membrane chamber.** Schematic comparison of assemblies for IEC

974   monolayer culture highlight that PET transwell membrane holders have a large plastic

975   support (A), which has been omitted in the novel AMCs (B). Both structures were placed

976   in a 35 mm glass bottom dish for imaging. The lower height of AMCs allows for closer

977   proximity, and thus greater numerical aperture, of the microscope's objective and

978   condenser. The optical interference caused by the large plastic transwell support and

979   resulting larger working distances of both objective and condenser is illustrated by live

980   cell imaging of infections in intact PET transwells in an inverted microscope (C,F,G)

981   versus cut-out PET membranes using an upright water-dipping microscope (D,H,I). This

982   change in microscope setup improved the lateral resolution of bacteria (*Salmonella*) on

983   the cell surface (F,H) and the apical surface topology of IECs (G,I). Either bacteria or

984   surface topology could be emphasized by slightly changing the focal plane, as indicated

985   on the right. Replacing the PET membrane with an alumina membrane held within the

986   custom-designed AMC (E) further improved the imaging resolution and minimized

987   optical interference (J,K). AMCs allow for sequential imaging of the same sample with

988   DIC and SEM (L-N). The latter confirmed that differentiated IECs grown in AMCs exhibit

989   a highly interconnected epithelium with a densely microvilliated surface. Bacteria are

990   indicated with yellow arrow heads. Overlaid dashed lines indicate cell-cell junctions.

991   White and yellow scale bars: 10 and 1 μm, respectively.

992

993   **Figure 2. Tracking of microbes on IEC monolayers using DIC imaging resolve**

994   ***Salmonella* and *Giardia* motility patterns.** Confluent, differentiated IEC monolayers in

995   AMCs were infected with *Salmonella-mCherry* (A-B) or *Giardia-mNeonGreen* (C-D).

996   The figure shows tracking from DIC time-lapse movies. Tracking using the respective

997   fluorescent markers (for validation purposes) is shown in Fig S2. DIC movies were

998   processed using a gaussian filter (DIC-GF) to remove uneven background illumination

999   and achieve optimal contrast for *Salmonella* (A, top panel) and *Giardia* (C, top panel).

1000   Subsequently, the total DIC-GF stack temporal median projection was subtracted from

1001   every frame to specifically emphasize moving structures (TM), and pixel values were

1002   squared (TM^2) to yield positive (white) pixels on a zero (black) background. The TM^2

1003   filtered time series was used to track all visible *Salmonella* using automated particle

1004   tracking (A, bottom panel). For *Giardia*, the TM filtered images were used for manual

1005   tracking of swimming trophozoites (C, bottom panel). A random sample of tracks within

1006   the field of view (FOV) was used to visualize *Salmonella* motility (B), while all manually

1007   tracked paths are shown for *Giardia* (D). The population mean and standard deviation

1008   for the track speeds were calculated based on all available tracks (Fig S2C,D). In A and

1009   C, a representation of the focal plane (red) is indicated on the right. Tracked microbes

1010   are indicated by magenta circles, tracks by continuous colored lines. Overlaid dashed

1011   lines indicate cell-cell junctions. Scale bars: 10 μm.

1012

1013   **Figure 3. *Salmonella* infection cycle stages at the apical IEC surface.** Differentiated

1014   IEC monolayers were infected with *Salmonella* and imaged every 15 s. *Salmonella* was

1015   most commonly observed to attach to the apical surface for the duration of the

1016   experiment (A). A fraction of bacteria was unsuccessful in establishing a lasting

1017   adhesion, seen as a short attachment and sudden disappearance (A, asterisk). In other

1018   cases, *Salmonella* disappeared from the surface after prolonged attachment either in

1019   the absence of visible IEC surface perturbation (B, top row panels), or concomitant with

1020   the induction of phenotypically small and discreet (B, middle row panels), or larger

1021   donut-shaped (B, bottom row panels) host cell invasion structures. *Salmonella* invasion

1022   elicited prompt extrusion of some targeted IECs (C, top panel), which involved an

1023   inward movement of the surrounding IECs, evident from an overlaid drawing of the cell-

1024   cell junctions (C, bottom panel). Throughout, a representation of the focal plane (red) is

1025   indicated on the right. Bacteria are indicated with yellow, and invasion structures with

1026   red arrow heads. Yellow asterisks indicate disappearing bacteria (detachment or

1027   invasion). Overlaid dashed lines indicate cell-cell junctions. Scale bars: 10 μm.

1028

1029   **Figure 4. *Giardia* trophozoite exploration of the IEC surface.** The link speeds of

1030   *Giardia* tracks from Fig 2C,D was analyzed (see also Fig S4) and a representative track

1031   showing the common circular pattern was plotted on the DIC (A, top panel) and TM

1032   filtered (A, bottom panel and enlarged crop) images. Upon inspection of link speeds, the

1033   trophozoite was found to swim with highly variable speeds within a single track (B). The

1034   mean, minimum, and maximum speed for this track are indicated (B). During planar

1035   swimming, the trophozoite intermittently paused upon sections of the epithelium (B,

1036   black arrows), in one location each of the four times the trophozoite visited that

1037   particular area (B, white arrow). Upon closer inspection of a single, attached trophozoite

1038   (C), the TM filtered time stack showed movement of individual flagellar pairs, which

1039   could be manually segmented to follow their shape and position over time (C, middle-

1040   and bottom panel to the right, respectively). In A, a representation of the focal plane

1041   (red) is indicated on the right. Tracked microbes are indicated by magenta circles,

1042   tracks by continuous yellow lines. Yellow- and red arrow heads indicate continuously

1043   attached and temporarily attached *Giardia* respectively. The enlarged trophozoite is

1044   indicated with a yellow square. Scale bars: 10 µm.
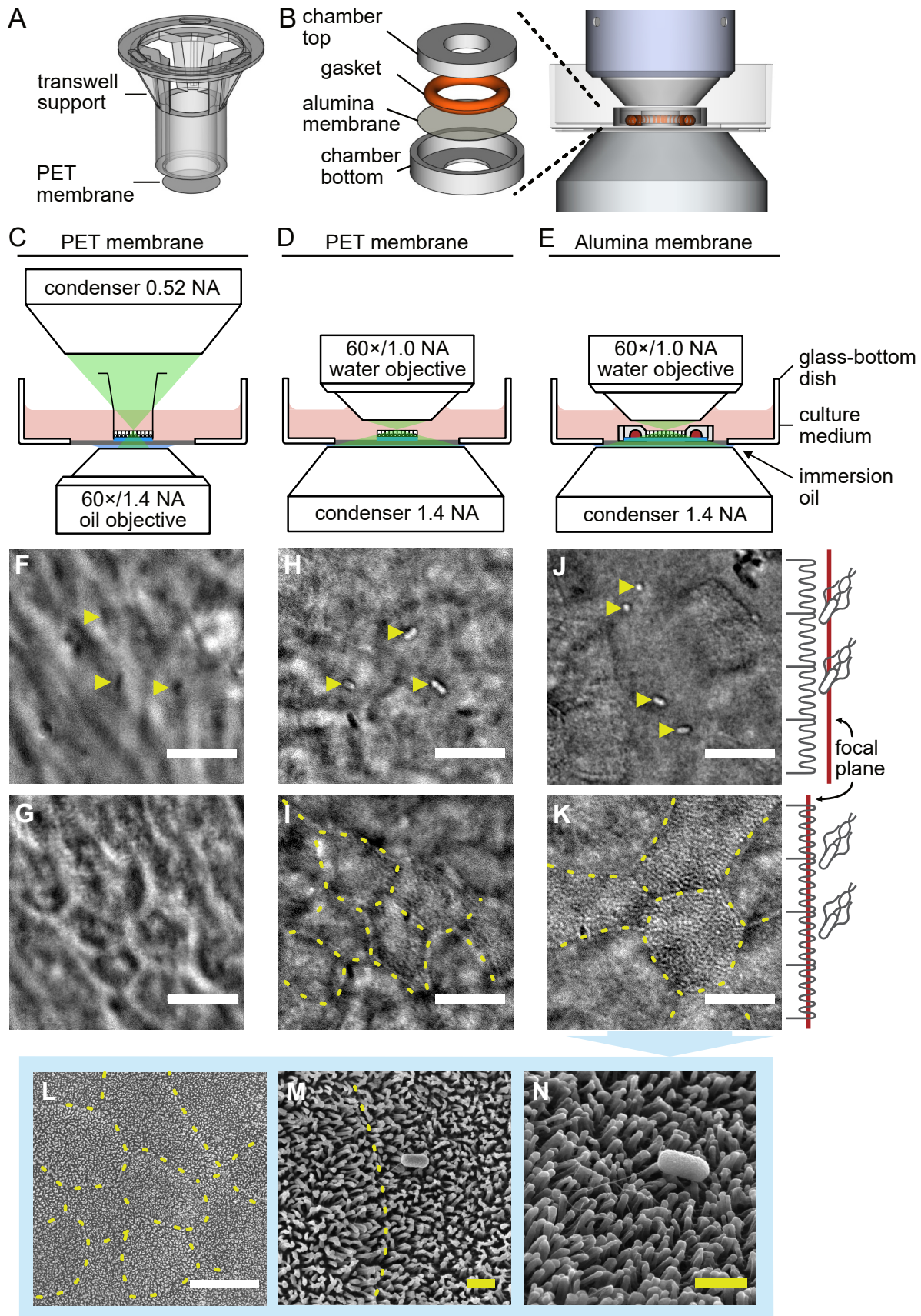
Figure 1. High-definition live cell DIC imaging of IEC monolayer infections in a novel alumina membrane chamber.
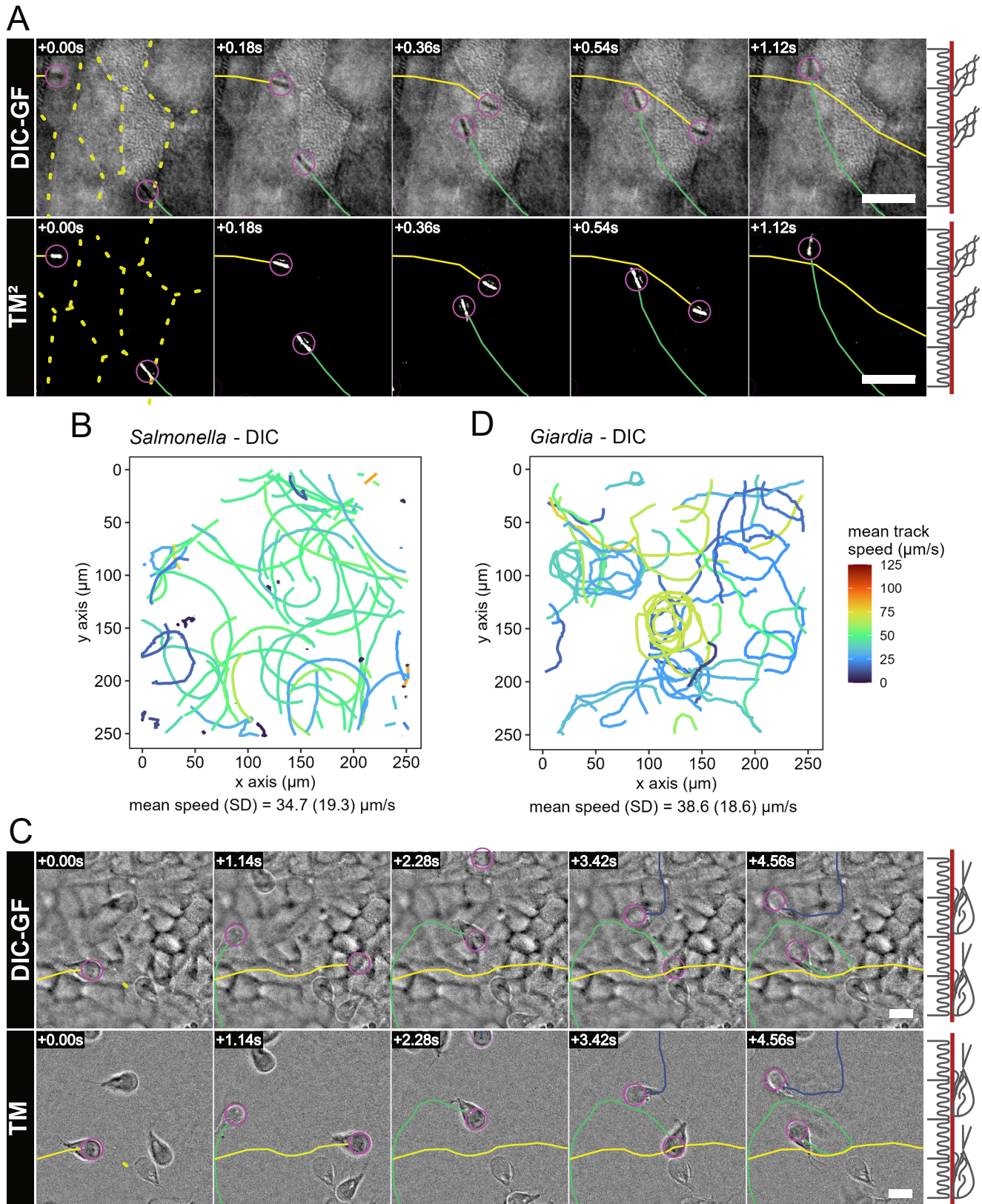
Figure 2. Tracking of microbes on IEC monolayers using DIC imaging resolve Salmonella and Giardia motility patterns.
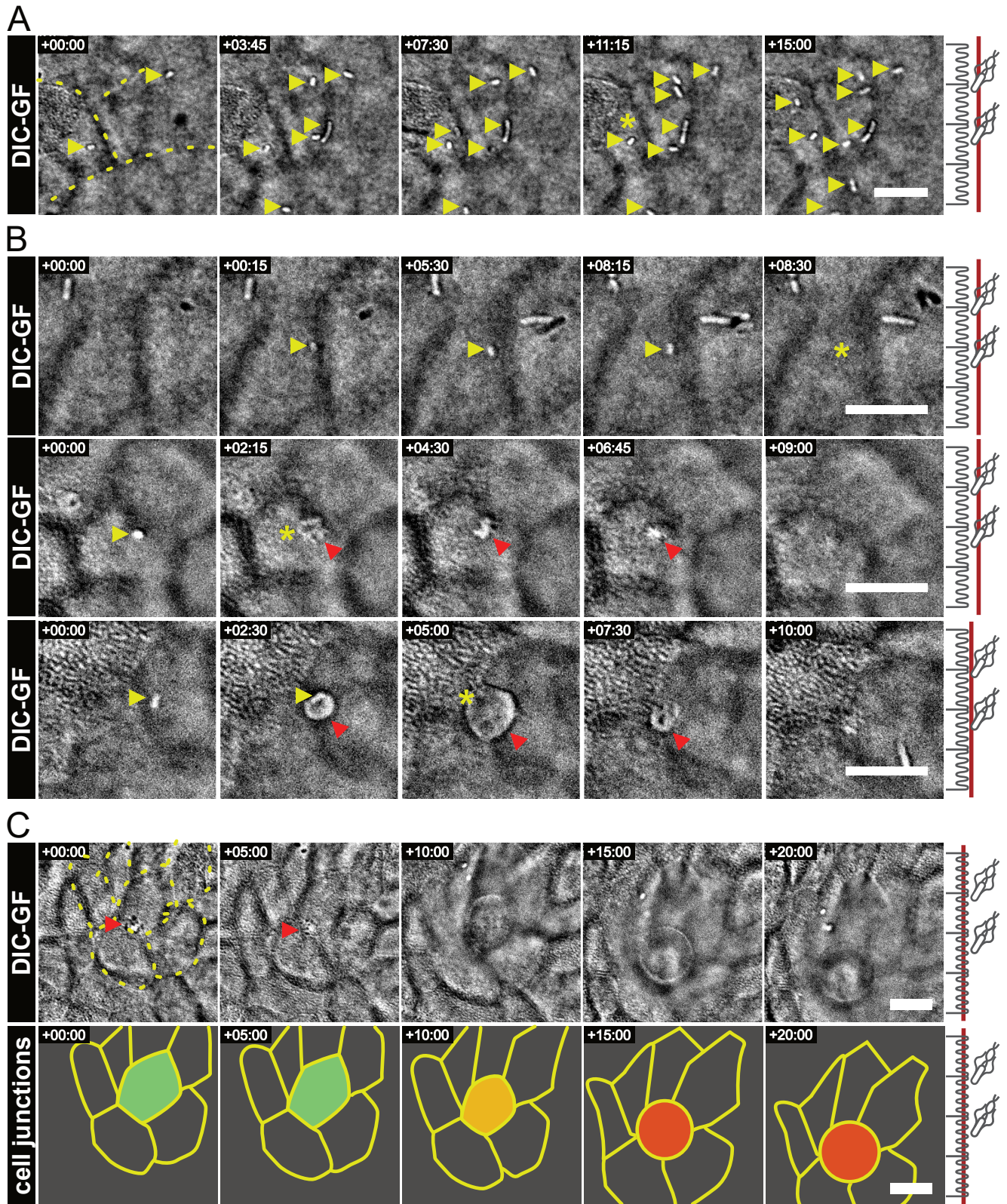
Figure 3. Salmonella infection cycle stages at the apical IEC surface.

mean speed (SD) = 36.42 (19.26) µm/s
min. speed = 0 µm/s
max. speed = 115.98 µm/s

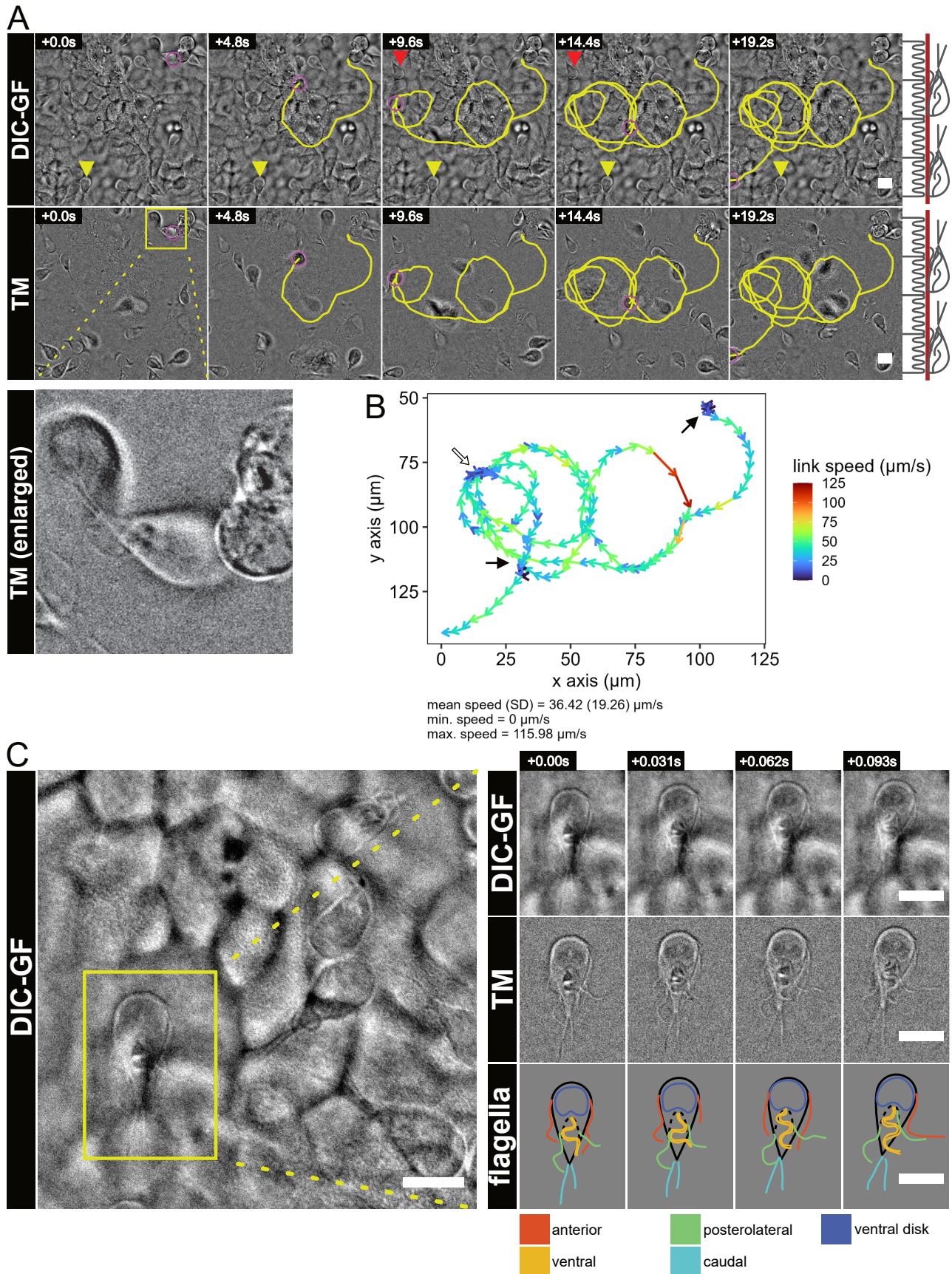anterior   posterolateral   ventral disk
ventral   caudal

Figure 4. Giardia trophozoite exploration of the IEC surface.